ChemSusChem

Research Article
doi.org/10.1002/cssc.202102506

Chemistry Europe
European Chemical Societies Publishing

www.chemsuschem.org

Copper Carbonate Hydroxide as Precursor of Interfacial CO in CO_2 Electroreduction

Shan Jiang,[a] Luca D'Amario,*[a, b] and Holger Dau*[a]

Copper electrodes are especially effective in catalysis of C_2 and further multi-carbon products in the CO_2 reduction reaction (CO_2RR) and therefore of major technological interest. The reasons for the unparalleled Cu performance in CO_2RR are insufficiently understood. Here, the electrode–electrolyte interface was highlighted as a dynamic physical-chemical system and determinant of catalytic events. Exploiting the intrinsic surface-enhanced Raman effect of previously characterized Cu foam electrodes, operando Raman experiments were used to interrogate structures and molecular interactions at the electrode–electrolyte interface at subcatalytic and catalytic potentials. Formation of a copper carbonate hydroxide (CuCarHyd) was detected, which resembles the mineral malachite. Its carbonate ions could be directly converted to CO at low overpotential. These and further experiments suggested a basic mode of CO_2/carbonate reduction at Cu electrodes interfaces that contrasted previous mechanistic models: the starting point in carbon reduction was not CO_2 but carbonate ions bound to the metallic Cu electrode in form of CuCarHyd structures. It was hypothesized that Cu oxides residues could enhance CO_2RR indirectly by supporting formation of CuCarHyd motifs. The presence of CuCarHyd patches at catalytic potentials might result from alkalization in conjunction with local electrical potential gradients, enabling the formation of metastable CuCarHyd motifs over a large range of potentials.

Introduction

The environmental and energy crisis drives researchers in pursuing novel clean energy strategies.[1] The electrochemical conversion of atmospheric CO_2 to valuable fuels is a promising approach that can help to mitigate anthropogenic carbon emission by storing renewable energy resources in chemical form.[2] Metallic Cu is the only pure metal that enables the production of multi-carbon products.[3] However, there is a variety of product of the CO_2 reduction reaction (CO_2RR) and the product distribution is usually quite diverse and rarely controllable.[3c,4] In order to boost C_{2+} product selectivity, various strategies have been explored, for instance, increasing the electrode surface roughness by making nanostructures,[5] preparing bimetallic catalyst,[6] or simple anodic preconditioning protocols.[7] The understanding of the mechanism of CO_2RR with special focus on the factors guiding selectivity is crucial for the development of a practical, large-scale catalyst.[8]

Oxide derived copper (OD–Cu) exhibits better selectivity for C_{2+} products.[7a,9] The mechanism behind the increased efficiency is still a question under debate.[10] It is believed that moderate CO surface adsorption facilitates C–C coupling in C_{2+} production.[8a,11] Verdaguer-Casadevall et al. proposed that strong binding sites for CO lie in the grain boundaries of OD–Cu, leading to further reduction of CO to C_{2+} products,[12] whereas Klingan et al. explained quantitative correlations between CO formation, surface-bound *CO and C_2H_4 formation by local alkalization.[13] Other reports claim "subsurface oxygen" can survive even under high catalytic (negative) potentials, which could help stabilize reaction intermediates.[14] It is not clear whether this effect is due to morphological reasons or specific oxo groups involved in the catalytic mechanism.[5b,9c] In any event, in recent reports Cu^+ is often considered as an active-site copper species,[7b,10a,15] and the synergistic effect of Cu^+ and Cu^0 may promote both CO_2 activation and the *CO dimerization.[10a,16]

Operando techniques can be used for mechanistic investigations since they give the opportunity to study the catalyst during operation.[17] In case of OD–Cu-driven CO_2RR, the need of operando measurements is intensified because of the instability of the Cu surface under non-operating conditions. Operando Raman spectroscopy is particularly suitable to study reactions on copper since roughened Cu enables the surface enhancement effect.[18] Indeed, this amplifies the signal of the molecules adsorbed on the surface of Cu such that even a single molecular layer can be detected.[18b,19] With the help of operando Raman spectroscopy researchers could trace reaction intermediates and catalyst oxidation states to gain insight on CO_2RR mechanism;[17g,20] for a discussion of adequate normalization of surface-enhanced Raman spectra and numerous

[a] S. Jiang, Dr. L. D'Amario, Prof. H. Dau
Department of Physics
Freie Universität Berlin
Arnimallee 14, 14195 Berlin (Germany)
E-mail: holger.dau@fu-berlin.de
[b] Dr. L. D'Amario
Department of Chemistry, Ångström Laboratory
Uppsala University
Box 523, 75120 Uppsala (Sweden)
E-mail: luca.damario@kemi.uu.se

Supporting information for this article is available on the WWW under https://doi.org/10.1002/cssc.202102506

operando spectra addressing CO_2RR at copper surfaces, see the report by Jiang et al.[21]

Chernyshova et al., using operando Raman spectroscopy, proposed that the first step of CO_2 reduction is a single-electron transfer to molecular CO_2 forming $*CO_2^-$, which adsorbs onto the Cu surface with the C and O atoms.[22] In a following work, the interaction of the co-adsorbed sodium cation to the proposed $*CO_2^-$ intermediate on Cu(111) surface in the presence of an electric field was also investigated by density functional theory (DFT) modelling, based on which a specific activation pathway of $*CO_2^-$ towards CO or formate has been postulated.[23] Although the formation of $*CO_2^-$ through molecular CO_2 has been considered energetically disfavored, the stabilization of $*CO_2^-$ may promote this reaction kinetically.[3a]

On the other hand, it is still unclear whether CO_2 gas or bicarbonate is the first reactant in CO_2RR. Dunwell et al. investigated the role of bicarbonate in CO_2 reduction on gold by isotope labelling of reactants.[24] It was found that the isotope content of the produced CO is largely unaffected (for the initial 20 min) when only CO_2 gas is marked, which suggests that CO_2 gas is not the C source of the reaction. However, they report that without purging CO_2 gas in the electrolyte medium, the pure bicarbonate buffer did not support any CO formation. Therefore, it was concluded that CO_2 (aq) in equilibrium with bicarbonate is the C source in CO_2RR. A similar result was reported for CO_2RR on Cu.[25]

Kortlever et al. proposed the direct reduction of bicarbonate on the Cu surface;[26] after using 1 M $KHCO_3$ without CO_2 gas purging, they detected formate as a product of CO_2RR. This evidence changed the assignment of the voltametric reduction at around -0.7 V_{RHE} (RHE: reversible hydrogen electrode) to bicarbonate reduction that had previously been assigned to *CO adsorption.[27] In the same study, different facets of metallic copper showed different activities; in particular the highly undercoordinated Cu(110) facet exhibited the highest reduction currents.[26]

Recently, malachite [copper carbonate hydroxide, $Cu_2(OH)_2CO_3$] nanorods have been proposed as the actual active species in Cu driven CO_2RR.[28] The malachite nanorods, spontaneously formed on copper foil, showed a greater activity than bare copper towards formation of C_2 compounds, suggesting that the copper carbonate hydroxide material could be the actual catalyst of the reaction.[29] In another study, Cu carbonate was observed on Cu^{2+} surfaces and assumed to block the CO_2 reduction reaction sites due to the poor charge transport.[15a] Notably, affinity of Cu oxides to organic material has also been investigated with regard to biomass waste treatment catalyzed by Cu anodes.[30] In such an environment, Cu carbonate was proposed as a passivating layer. In summary, to date there is no consensus on whether bicarbonate directly participates in CO_2RR or simply works as a buffering electrolyte with the carbonate ions in equilibrium to CO_2.[25,31]

Herein, we use operando Raman spectroscopy to study the electrode/electrolyte interface prior and during CO_2RR catalysis with the aim to characterize the catalytically active material. We show formation of amorphous copper carbonate hydroxide layers locally resembling the mineral malachite, where the carbonate ions of the malachite-like material likely can be reduced directly to carbon monoxide. This observation and comprehensive sets of complementary experiments suggest a central role of bicarbonate in the CO_2 reduction reaction and help explaining the higher activity of oxide-derived Cu for CO_2 reduction.

Results and Discussion

Overview of copper-foam redox chemistry

Copper electrodes were prepared as described in the Experimental Section and left under atmospheric condition overnight, during which time a layer of copper oxide is naturally formed on the surface. Due to their porous structure described elsewhere,[13] they are denoted as Cu foams. As shown in Figure 1, a cyclic voltammogram (CV) of such Cu foam electrode, in a CO_2-saturated bicarbonate buffer solution, shows unstructured, reversible as well as irreversible reduction and oxidation peaks. Clearly, this behavior reflects the complex nature of the CO_2RR, oxide reduction, and other reactions occurring at the oxide-derived Cu surface, as detailed further below. When a constant potential is applied for about 20 s, the current level stabilizes (see Figure S2) suggesting that the system is sufficiently close to a steady state. This allows for collection of reproducible surface-enhanced Raman scattering (SERS) spectra, which facilitates systematic examination of the surface composition of the catalytic electrode and its interface with the electrolyte.

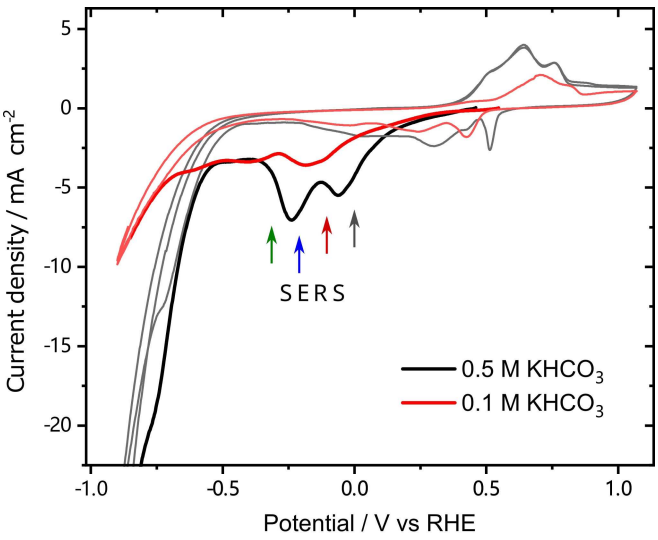

Figure 1. Cyclic voltammetry of Cu foam measured in CO_2 saturated 0.1 M (red) and 0.5 M (black) $KHCO_3$, 10 $mV s^{-1}$. Thicker lines highlight the first sweep from open-circuit potential to first vertex. Arrows indicate the potential where operando SERS shown in Figure 2 was performed, from right to left: 0, -0.1, -0.2, and -0.3 V_{RHE}.

Operando Raman spectra in CO_2-saturated carbonate electrolyte

SERS measurements were performed on a Cu-foam electrode recording for 2 min at the respective electric potential, starting 20 s after a potential change. In the following, unless otherwise specified, we will refer to this measurement protocol simply as "operando" (product composition analysis via gas-chromatography of the same system published elsewhere, see ref. [13]). Typical operando SERS spectra, from 0 to −0.3 V_{RHE} (see arrows in Figure 1), of Cu foam electrode for CO_2 reduction are shown in Figure 2, where 0.1 M $KHCO_3$ saturated with CO_2 was used as electrolyte; spectra collected over a larger range of potentials, 0 to −0.6 V_{RHE}, are reported in Figure S1 in the Supporting Information. Prior to application of any potential (open-circuit potential, OCP), the only peaks present are at 405, 520, and 620 cm^{-1} (see Figure S1), which have been assigned to a mixture of Cu_2O, CuO, and $Cu(OH)_2$, as they are formed on the surface of metallic Cu after being exposed to air.[13,32] After sequential application of increasing negative potentials from 0 to −0.3 V_{RHE}, peaks at 354–305 (A), 705 (B), 1070 (C), and 1533–1512 cm^{-1} (D) appeared, and a shoulder peak at 1045 cm^{-1} (C1) and two less prominent peaks at 1340 and 1677 cm^{-1} (D1 and D2 respectively) are visible. Peak A may comprise two overlapping peaks, which evolve differently with applied potential: the 354 cm^{-1} peak dominates at −0.1 V_{RHE}, with a shoulder at 305 cm^{-1}, which grows at larger potentials and becomes the dominant peak at −0.4 V_{RHE}. The peak at 1070 cm^{-1} is usually assigned to carbonate symmetric stretching.[33] The assignment of the other peaks is unclear, yet their simultaneous appearance suggests that they could belong to the same species. Moreover, these peaks are observed at the oxide reducing potentials and the increase of peak (B) and (D) seems to occur concurrently to the oxide peak weakening, suggesting a relation between the two phenomena. Interestingly, at the same time a peak at 2040–2080 cm^{-1}, usually assigned to adsorbed CO,[20a,c,d,21] arises, which is not expected at these low overpotentials ($E^{\circ}_{CO_2/CO}$ = −0.10 V_{RHE}).[4] The assignment of this peak is confirmed by a similar experiment performed substituting H_2O electrolyte with D_2O, where the 2040–2080 cm^{-1} peak was still observed, excluding the attribution to H adsorption (see Figures S1, S34, S36). There is also evidence for CO_2 reduction products aside from CO, namely the presence of C–H bands (Figure S1), mainly corelated to the formation of formic acid and other C_1 and C_2 products.[21]

Operando Raman or IR spectroscopy have been used by several researchers investigating CO_2 reduction on Cu catalysts.[20c,21,22,34] The peaks at 705 and 1530 cm^{-1} have been assigned to in-plane bending and asymmetric stretching of a $*CO_2^-$ intermediate (bound to Cu surface with C and O) produced by a singly reduced CO_2 molecule.[22] In the following, we will analyze the relation of the peaks A–D to the CO_2RR.

Influence of carbonate concentration in CO_2-depleted electrolyte

The operando experiment of Figure 2 was performed again but without CO_2 saturation of the electrolyte. Therefore, a nitrogen gas stream was used for purging the electrolyte, and SERS spectra were collected in 0.1 and 1 M bicarbonate electrolyte (Figure 3). We note that removal of CO_2 alters the bicarbonate buffer equilibrium such that the pH of the solution changes from 6.8 with CO_2 saturation to about 9 with N_2 saturation (for 0.1 M $KHCO_3$). This pH change easily could alter the affinity of the Cu surface regarding reactions intermediates or any adsorbed chemical species, as discussed further below in more detail. Yet the main objective of the experiment is to examine the influence of the bicarbonate concentration in the absence of gaseous CO_2. The presence of residual dissolved CO_2 deriving from the equilibrium with (bi)carbonate is excluded due to the continuous N_2 purging. The results, reported in Figure 3 (solid line spectra; see Figure S5 for 0.5 M $KHCO_3$), show that in N_2-saturated 1 M $KHCO_3$ (pH 8.7), the peaks A–D are visible and present an increased intensity in the 0 and -0.1 V_{RHE} spectra. We conclude that bicarbonate itself, in the absence of dissolved

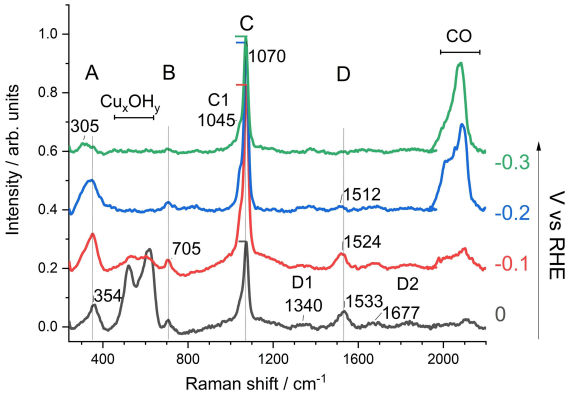

Figure 2. Operando SERS spectra of Cu foam in CO_2-saturated 0.1 M $KHCO_3$ (pH 6.8) at various potentials (from 0 to −0.3 V_{RHE}). Due to peak position shift with increasingly negative potentials, we label peak ranges of interest with A for the peak(s) at 354–305 cm^{-1}, B for the peak at 705 cm^{-1}, C for the peak at 1070 cm^{-1}, and D for the peak at 1512–1533 cm^{-1}.

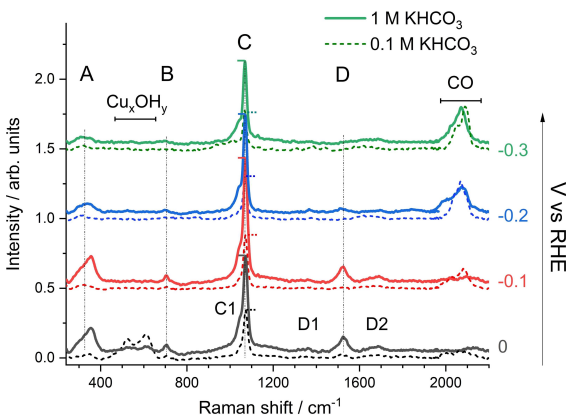

Figure 3. Comparison between operando SERS spectra of Cu foam measured in N_2-saturated 0.1 M $KHCO_3$ (pH 9.16) (solid line) and 1 M $KHCO_3$ (pH 8.7) (short dash line) at various potentials (from 0 to −0.3 V_{RHE}). Complete data is also shown in Figures S3 and S4.

CO_2, can produce the species responsible for peaks A–D. The presence of the CO stretching band indicates that CO_2 gas purging is not required for CO formation. Worth noting, without CO_2, in highly concentrated bicarbonate buffer, hydrogen evolution is facilitated, as conspicuous bubble formation was observed at potentials lower than −0.4 V_{RHE}. Nevertheless, spectroscopic evidence of hydrogen adsorption was never found.

^{13}C isotope labelling of the bicarbonate/CO_2 electrolyte

Selective ^{13}C isotope labelling was performed on the bicarbonate/CO_2 mixture of the electrolyte. This experiment was conducted in the shortest time possible (typically 10 min CO_2 solution saturation prior measurement, plus 8 min measurement time) to avoid isotope mixing due to the equilibration of the bicarbonate/CO_2 system (see Figure S6 for more details). The labelling of $KHCO_3$ (but not of the CO_2 gas) produces a frequency shift of peak D from 1533–1505 to 1497–1474 cm^{-1} (Figure 4, see Figure S7 for details; further dataset in Figures S8 and S9). It can be noted that the weaker peaks, D1 and D2, shift to a similar extent as the main peak D. Labelling instead solely CO_2 does not cause any shift of peak D (see Figure S10), which again supports that the primary source of this band are bicarbonate ions. The isotopic shift is consistent with C–O vibration from either $*CO_2^-$[22] or a carbonate anion.[24–25] Further below, we will propose assignment to a copper carbonate hydroxide species. The band at 705 cm^{-1} shows no clear shift as displayed in Figure S7. The CO band is significantly modified by $^{12}C/^{13}C$ exchange, but a quantifiable band shift cannot be resolved because of the complexity of the CO bandthat comprises several sub-bands of varying amplitudes. Notably, a clear shift of the CO peak can be observed by applying the potential further to −0.7 V_{RHE} but only within about 10 min of operation, until the ^{13}C-atoms of carbonate are mostly exchanged with the C-atoms from $^{12}CO_2$ (Figures S11–15).

We also cannot resolve a clear shift of peak A at 350 cm^{-1} in ^{13}C-labelled electrolyte (Figure 4, Figure S7 for details; further dataset in Figures S8 and S9). Due to the absence of clear frequency shift upon electrolyte labelling with ^{13}C, we propose to assign peak A to a Cu–O vibration. Moreover, as described in the following, a similar peak was observed in operando SERS recorded with carbon-free phosphate buffer, which strongly supports the assignment to Cu–O vibrations.

Comparison with phosphate electrolyte

In phosphate electrolyte, the peak at 310 cm^{-1} is visible together with bands of adsorbed phosphate ions at 800–1100 cm^{-1} (Figure 5). Gediminas et al. have investigated phosphate adsorption on Cu, Ag, and Au with operando Raman.[35] They observed a peak at around 320 cm^{-1} on Cu surface as well as a phosphate band, similar to the spectra in Figure 5, and suggested that phosphate adsorbs through a bridging oxygen.[34] To be noted, it is common also for other oxyanion to adsorb on Cu and noble metal surfaces through the oxygen atom.[36] The M–O vibration, in these cases, typically appears in the 250–400 cm^{-1} region.

The operando SERS recorded in phosphate buffer show a correlation between applied potential and the relative amplitudes of the phosphate bands. The more negative the potential the stronger is the signal from deprotonated phosphate species (see 987 cm^{-1} HPO_4^{2-} vs. 1103 cm^{-1} $H_2PO_4^-$ in Figure 5), suggesting pronounced alkalization at the electrolyte–electrode interface. Noteworthy, a CO signal appears in the −0.3 V_{RHE} spectrum, which was not expected due to the absence of a carbon source in the electrolyte. The appearance in only one operando spectrum is an indication that it originates from a small amount of material (see also Figure S17). Thus, this peak was attributed to traces of carbonate deriving from unavoidable sample exposure to air.

The results presented so far support that the CO_2RR intermediate visible in the operando SERS are related to

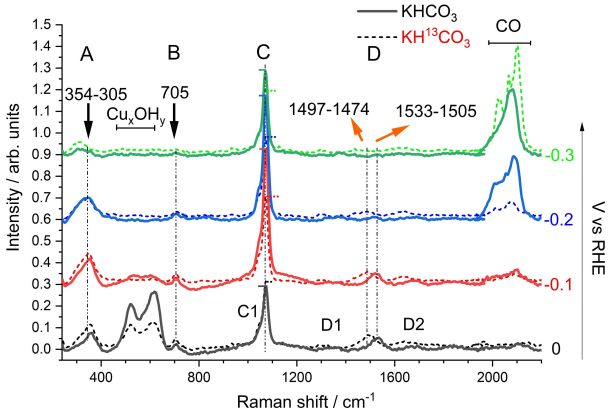

Figure 4. Comparison between operando SERS spectra of Cu foam measured in CO_2 saturated electrolyte with 0.1 M $KH^{12}CO_3$ (solid lines) and 0.1 M $KH^{13}CO_3$ (pH 6.8) (dashed lines) at various potentials (from 0 to −0.3 V_{RHE}). A peak comparison is also shown in more detail in Figure S7.

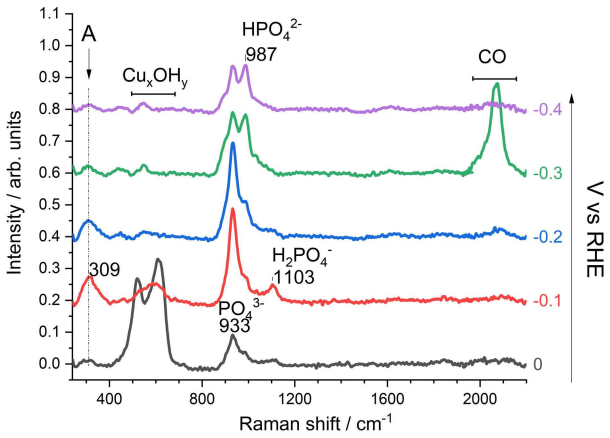

Figure 5. Operando SERS spectra of Cu foam measured in N_2-saturated 0.1 M potassium phosphate buffer (pH 6.8) at various potentials (from 0 to −0.4 V_{RHE}). Complete data see Figure S16. Repetition see Figure S17.

carbonate species rather than being created by reduction of dissolved CO_2. For clarity purposes, the discussion that follows starts with a comparison of our already presented results with some literature reports, trying to address inconsistencies, in particular regarding the assignment of spectroscopic signatures to either adsorbed CO_2 or carbonate or products of their reduction. Afterwards, the discussion continues with an analysis of what are thermodynamically and kinetically conceivable events in our experiments, proposing a new way to interpret the operando SERS data, which further below will be supported by additional experiments. We believe that the interpretation proposed herein can support an adequate discussion of Raman CO_2RR data, potentially changing the future course of interpretation in terms of reaction mechanisms.

Peak D is not assignable to adsorbed (bi)carbonate

In the following it is shown that peak D at 1530 cm^{-1} does not originate from vibration of adsorbed (bi)carbonate. We have listed and compared the peak positions from our experiment with other literature-reported carbonate bands in these regions in Table 1. We note that peak 1045 cm^{-1} was reported as –OH band in azurite and malachite.[37]

Dissolved solution species of (bi)carbonate have no bands at around 1530 cm^{-1}.[33] However when carbonate adsorbs on Au surface, it is reported to have bands at around 1429–1499 cm^{-1},which might be a possible explanation for peak D.[38] Peak D has been observed before in operando vibrational spectra of CO_2RR in bicarbonate buffer,[20c,d,22,24,34c,39] mostly assigned to carbonate anion adsorption.[20c,d,24,34c,39a] Exceptions are some reports that considered the potential correlation to CO_2RR intermediates.[22,39b,c] Absence of the peak at 1530 cm^{-1} (D) in the clear presence of an adsorbed carbonate band at 1068 cm^{-1} (C) disfavors assignment of peak D to adsorbed carbonate.[22] We observed the same behavior in our experiment performed in N_2-saturated 0.05 M K_2CO_3, where peak D was not observed while the band at 1070 cm^{-1} band was clearly present (Figure S18). In all the experiments described herein, the correlation between the presence of peak C and D is not biunivocal: The band of adsorbed carbonate is always present when also peak D is, but peak D may be absent in the presence of a carbonate peak. We believe that peak C does not simply originate from carbonate adsorption to a metallic copper surface. There could be two carbonate species contributing to the comparably broad asymmetric vibrational band of peak C, with one species giving rise also to peak D. We note that the correlation between the oxide and the appearance of peak D is crucial to unravel its origin. As shown further below, the occurrence of peak D correlates with the disappearance of oxide bands.

Table 1. Summary of Raman shifts (wavenumber in IR if labelled) for various carbonate species from literature and present study.

Species	Raman shift/wavenumber [cm^{-1}]				Ref.
present study	705	1045	1068	1500–1530	this work
CO_3^{2-}(aq)	684	–	1064	1430–1380	[33]
HCO_3^-(aq)	632, 672	1017	–	1360, 1630	[33]
azurite	765, 739	1035	1090	1578	[37]
malachite	765, 719	1045	1101, 1058	1492	[37]
carbonate on Au (SNIFTIR)	–	–	–	1425–1499	[38]
Sn-carbonate (IR)	–	–	–	1500	[39c]

Equilibrium phases and formation of a metastable material

Mostly operando Raman spectroscopy results on CO_2RR are evaluated on the basis that the rough Cu surface can enhance the signal of adsorbed molecule. However, the measured Raman signals do not necessarily imply that the detected peaks are indeed stemming from individual molecular species adsorbed directly on the metallic copper surface. The surface Raman enhancement effect can extend over several nm.[40] Several layers of material on the copper surface could be either detectable due to the enhancement effect of the Cu surface or because of their intrinsic Raman properties. Indeed, an estimation of the charge exchanged in the reduction of a monolayer of adsorbed species results in a 1/30 of the redox charge that we typically obtain by integration of CV waves (see Figure S19 for more details). These figures imply that a quantity of material clearly exceeding a single monolayer needs to be adsorbed on the Cu surface to explain the observed current densities. In the following we discuss that metastable materials may be produced at the Cu surface under CO_2RR operation conditions.

Analysis of the thermodynamics of the system hints at possible chemical species that can be formed around the Cu electrode. Pourbaix diagrams show the thermodynamically stable species as a function of E_m, the applied electric potential or solution redox potential, and pH. Since the studied system is a copper electrode immersed in a bicarbonate solution, the Pourbaix diagram of Cu/Cu_2O/azurite/malachite in Figure 6A is of relevance. In Figure 6A, the blue square marks the electrochemical potential of the CO_2 saturated 0.1 M bicarbonate solution used herein in most experiments ($\approx$1.1 V_{RHE}, experimentally determined under CO_2 purging,[41] see Supporting Information for detail), while the red circle indicates the Cu foam electrode system position at OCP ($\approx$0.5 V_{RHE}). The yellow star depicts the electrode potential at 0 V_{RHE} (at pH 6.8).

The as-deposited Cu electrodes are covered by a layer of Cu_xOH_y, which forms readily in air, as previously confirmed by X-ray absorption spectroscopy[13] and Raman spectroscopy (at OCP, see Figure S1). Thus, upon exposure to the bicarbonate buffer but prior to applying an electrode potential, the system can be considered as a phase of Cu (hydr)oxide interfaced with a bicarbonate electrolyte. This system is out of equilibrium (see Figure 6A, the difference between the red circle at OCP and the blue square), with a spontaneous tendency to convert the Cu_xOH_y into azurite/malachite. Related out-of-equilibrium considerations may be of relevance also when discussing the behavior upon application of an electrode potential (region

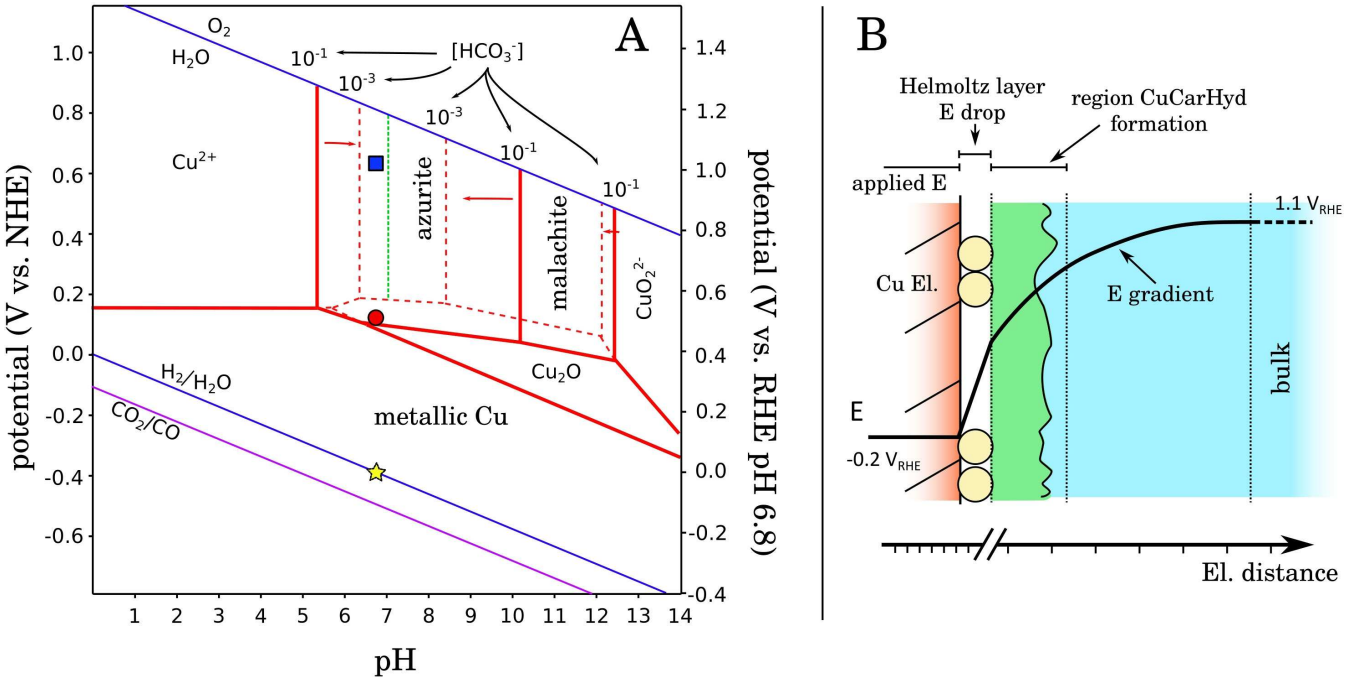

Figure 6. (A) Pourbaix diagram of the Cu–HCO_3^- solution system. The solid red lines represent a HCO_3^- concentration of 10^{-1} M, the dashed line a concentration of 10^{-3} M. The concentration of dissolved Cu^{2+} is also assumed to be 10^{-6} M, to account for equilibration of the $Cu/Cu(OH)_2$ with the electrolyte. The violet line represents the equilibrium potential of the CO_2/CO reaction. The green dashed line represents the minimal HCO_3^- concentration (HCO_3^- $10^{-4.3}$) needed to produce an azurite phase at any pH/potential. The blue square corresponds to the potential of a solution of CO_2 saturated solution of 0.1 M $KHCO_3$ (determined experimentally vs. a reference electrode by a Pt wire immersed in such solution).[41] The red circle indicates the open-circuit potential we typically observe for the as-prepared Cu foam. The yellow star indicates the zero level of the electric potential when using an RHE scale (0 V_{RHE} at pH 6.8). The blue solid lines represent the equilibrium potentials for reduction/oxidation of water. Diagram based on ref. [42]. (B) Graphical representation of the electrical potential vs. distance from the electrode surface under cell operation; Cu electrode in red, CuCarHyd in green, adsorbed species in the Helmholtz layer are shown as circles. A hypothetical potential profile is schematically shown for application of −0.2 V_{RHE}.

between yellow star and blue square in Figure 6A). During the application of a potential at the electrode, a gradient of the electrochemical potential forms due to the potential difference between negative electrode and the more positive electrolyte bulk ($\approx +1.1$ V_{RHE}). We propose a potential gradient as schematically shown in Figure 6B. A large part of the potential gradient is observed in the first layer of adsorbed material (Helmholtz layer). Even at potentials large enough to enable CO_2RR operation [i.e., −0.2 V_{RHE} (1.3 V difference from the bulk)], the electric potential that results after the first drop can be positive enough to allow, in conjunction with local alkalization, the formation/presence of oxidized species like a Cu carbonate hydroxide or Cu_xOH_y.

Malachite formation for copper foams in carbonate electrolyte

Clearly the system consisting of Cu oxide covered foam electrode immersed in carbonate buffer (and not exposed to any electrical potential, OCP conditions), can and will evolve naturally into a copper carbonate hydroxide phase. Indeed, for oxide-covered Cu electrode left for 6 days in 0.1 M $KHCO_3$, a green layer of substance evolves inside the cavities of the Cu foam electrode. The Raman spectrum of such a sample is compared to reference spectra of azurite and malachite in Figure 7A. For comparison, the 0 V_{RHE} spectrum taken from Figure 2, and a ^{13}C labelled sample (prepared in 0.1 M $KH^{13}CO_3$ for 6 days), are shown in Figure 7A as well.

The Raman spectrum of the green material (GM) formed after 6 days exhibits clear similarity with the malachite spectrum: all malachite peaks are detectable in GM, where additionally also Cu (hydr)oxide peaks are present at wavenumbers below 700 cm^{-1}, suggesting formation of malachite coexisting with (hydr)oxide phases. The coexisting malachite and the Cu (hydr)oxide likely may be spatially separated, as suggested by the microscope image of Figure S39. Also, the spectrum measured at 0 V_{RHE} exhibits remarkable similarities with the malachite spectrum. The material formed on the Cu electrode at 0 V_{RHE} may not closely resemble the crystalline malachite that is taken as a reference. However, considering the amorphicity of the copper carbonate hydroxide product resulting from conversion of the rough Cu (hydr)oxide layer, we can expect some shift in the vibrational frequencies and band amplitudes.

The extended X-ray absorption fine-structure (EXAFS) spectrum of a malachite-enriched sample resembles the malachite reference spectrum closely (Figure S21), which confirms that by long-term exposure to a carbonate-containing electrolyte the Cu material was completely transformed into malachite. Mala-

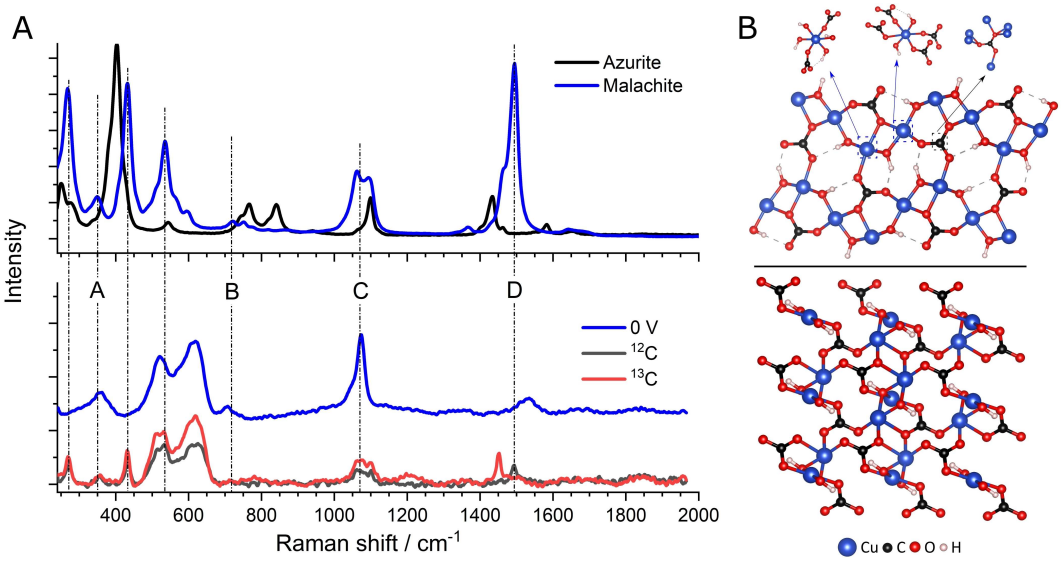

Figure 7. (A) Upper panel: reference spectra of azurite and malachite (from RRUFF database: ID R050497 and ID R050508, respectively); lower panel: SERS spectra of the green material, which we identify as malachite, formed from Cu-oxide covered electrodes upon exposure for 6 days in 0.1 M $KH^{12}CO_3$ (grey line) and $KH^{13}CO_3$ (red line) electrolyte, under OCP conditions, in comparison to spectrum of Cu foam equilibrated in CO_2 saturated 0.1 M $KH^{12}CO_3$ at 0 V_{RHE}. (B) Molecular structure of malachite, $Cu_2(OH)_2CO_3$(upper panel), and azurite, $Cu_3(OH)_2(CO_3)_2$(lower panel), remade based on ref. [43].

chite formation on Cu foam surfaces were not detected on the time scale of the in-situ EXAFS experiment, presumably because the transformation towards malachite involved only a minor material amount so that metallic Cu dominated the EXAFS spectra. This emphasizes the need to use surface-sensitive techniques. Nevertheless, conversion of oxide-enriched Cu sample to malachite under OCP conditions were observed by in-situ EXAFS (Figure S22), suggesting a material-transforming interaction of the Cu oxide with carbonate ions.

We conclude that rather than crystalline malachite, the material formed at 0 V_{RHE} may be a copper carbonate hydroxide with malachite-derived structural motifs.

Malachite-derived structural motifs in the catalytic potential regime

To illustrate and support the concept of a malachite-derived structural motif, we compare the Raman spectra of azurite, $Cu_3(OH)_2(CO_3)_2$, and malachite, $Cu_2(OH)_2CO_3$ (black and blue lines in Figure 7A upper panel, crystalline structures are also shown in Figure 7B). Even though the materials are quite similar in structure, some peak frequencies shift by 100–200 cm^{-1}. In the same fashion, the amorphous copper carbonate hydroxide that forms in our experiment could exhibit comparable shifts with respect to the crystalline reference materials. Moreover, we note that a shift of 40 cm^{-1} can be seen in the 1500 cm^{-1} peak of the ^{13}C samples compared to the ^{12}C samples in Figure 7A, which is comparable with the isotope shift of the Cu electrode reported in Figure 4. The isotope labelled sample further emphasizes the peak assignment at 1500 cm^{-1} to anti-symmetric stretching vibration of carbonate in this kind of structure. No clear shift of the peak at 350 cm^{-1} is observed, which further supports its assignment to Cu–O. Further experiment with a D_2O-labelled malachite sample showed only a peak shift at 430 to 420 cm^{-1}, which suggests a component of Cu–OH vibrations (Figure S20).

Due to spectral similarities and to comparable isotope peak shift we propose that the material detected in our measurements that is associated with the 1500 cm^{-1} band is an amorphous malachite-like copper carbonate hydroxide (CuCarHyd). Consequently, following previous assignments,[37] we assign peaks A–D as follows: A to X–Cu–O bending; B to in-plane bending of carbonate, ν4; C to C–O symmetric stretching of carbonate, ν1; D to anti-symmetric stretching of carbonate, ν3. It should be noted that the shift reported in the ^{13}C-labelling experiments of Figures 4 and 7A is in line with this assignment.

To support the relation of the spectra to a malachite-like material, we consider the measurements under nitrogen atmosphere (without CO_2 saturation) performed with different concentration of HCO_3^-. The electrolyte pH was not 6.8 but around 9, due to the absence of a CO_2 supply. Looking at the Pourbaix diagram, the driving force for the copper carbonate hydroxide formation increases slightly with higher pH. Furthermore, at higher concentration of HCO_3^- the stability region of Cu_2O is reduced (see dashed vs. solid lines) such that the CuCarHyd becomes the main stable compound in the range 0–0.4 V_{RHE} (i.e., the oxide can be converted into CuCarHyd). This explains why in Figure 3 the copper carbonate hydroxide is seen only in the high-bicarbonate experiment (1 M instead of 0.1 M $KHCO_3$).

Local alkalization during catalytic operation

The correlation of high pH with the stability of CuCarHyd opens an alternative path for its in-situ formation. During the oxide reduction process protons are consumed, causing a substantial variation of the local pH in proximity of the electrode. Such local alkalization could initiate the formation of metastable malachite-like material during operation. The extent of such local pH rise was probed through a series of operando Raman spectra using the 473 nm laser (see Figure S23), for which the SERS effect is negligible, thereby eliminating the signal from the surface-adsorbed species. In Figure S23, a clear local alkalization under oxide reduction potentials can be observed by the conversion of the HCO_3^- bands to the CO_3^{2-} bands. The CO_2/HCO_3^-, HCO_3^-/CO_3^{2-}, and H_2CO_3/HCO_3^- equilibria are sensitive to pH, and the HCO_3^- (1015 and 1356 cm^{-1}) and CO_3^{2-} (1068 cm^{-1}) band ratio changes accordingly. With this method the local pH under oxide reduction potentials is estimated to be around 9.5 (Figure S24), which is even larger than the one obtained with the 1 M bicarbonate solution that showed presence of CuCarHyd in Figure 3.

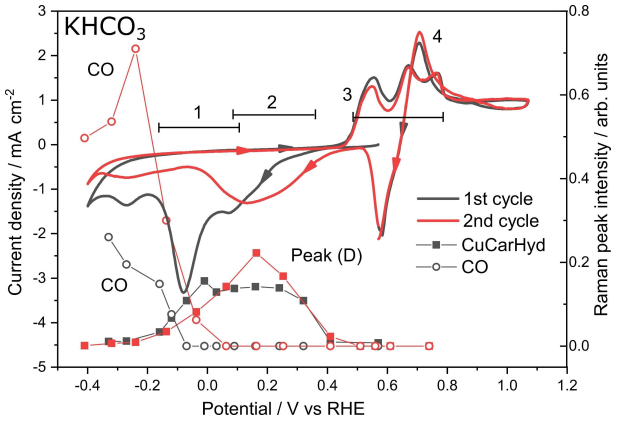

Figure 8. First (grey solid line) and second cycle (red solid line) of CV (1 $mV\,s^{-1}$) of Cu foam electrode measured in N_2-saturated 0.5 M $KHCO_3$ (pH 8.7) (left *y*-axis). The scan directions are indicated by arrows; the magnitude of peak D at 1530 cm^{-1} (square symbol solid line curve) and CO peak (empty circle line curve) in the operando Raman spectra are indicated (right *y*-axis). These peak intensities were determined from Raman spectra collected for 10 s while scanning the electric potential at a scan rate of 1 $mV\,s^{-1}$ (so that each spectrum corresponds to a potential range of 10 mV only). Redox wave assignment: 1, reduction of CuCarHyd; 2, reduction of Cu hydroxide; 3, Cu oxidation; 4, pitting corrosion.

CuCarHyd formation traced by CV currents

We propose that even a bare Cu electrode, in presence of Cu_xOH_y, can form a copper carbonate hydroxide layer detectable with SERS. In the following experiments, we address two questions: (i) is the CuCarHyd material formed before or during operation at catalytic potentials; and (ii) is the CuCarHyd promoting CO_2 reduction.

Three kinds of samples were prepared to investigate the source of the carbon necessary to form the CuCarHyd:

I. standard type of Cu foam electrode as used also further above (in contact with air);
II. Cu foam electrode left for 6 days in carbonate solution (malachite enriched);
III. Cu foam electrode left with a water layer on the surface for 4 days in a CO_2-free environment (hydroxide enriched).

Operando Raman spectra registered during CV were used to correlate the formation/consumption of the CuCarHyd layer with the formation of adsorbed CO. The above three types of Cu foam electrodes were each operated in:

(i) N_2-saturated bicarbonate solution;
(ii) Alkaline electrolyte (0.1 M KOH) without any carbonate/CO_2, to assess whether the formation of the CuCarHyd layer happens during or prior to operation.

Here, we specifically aim at investigation of the carbon source of the produced CO. Therefore, in the here-described CV experiments, the operating conditions of a real CO_2RR reactor (i.e., CO_2 saturated bicarbonate solution) were purposely not chosen. CV was recorded at a low scan rate (1 $mV\,s^{-1}$) starting from the OCP of the respective Cu foam electrode and spanning the range from −0.4 to 1.1 V_{RHE} (−0.6 to 1.5 V_{RHE} in KOH electrolyte). The low scan rate facilitated recording of operando Raman spectra (10 s acquisition time) around the various key points of the CV (every 50–100 mV). In Figure 8 (standard Cu foam in N_2-saturated bicarbonate buffer) and Figure 9 (malachite Cu foam in N_2-saturated KOH buffer), the first and second CV cycle are remarkably different in the cathodic regime (see Figures S25 and S26 for further details). In Figure 9, the waves look shifted due to the large charge exchanged, the onset potentials remain similar. In the first cycle the large reduction peak, with an onset around −0.1 V_{RHE}, is completely irreversible in Figure 9 but only partially in Figure 8. This means the

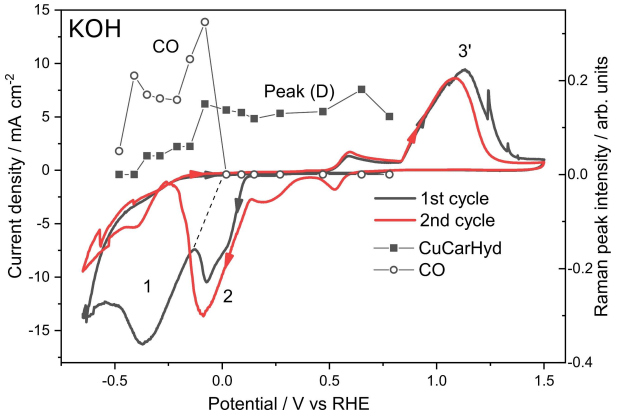

Figure 9. First (grey solid line) and second cycle (red solid line) of CV (1 $mV\,s^{-1}$) of Cu formed malachite electrode measured in N_2-saturated 0.1 M KOH (pH 13) (left *y*-axis), the scan directions are indicated by arrows; the magnitude of peak D at 1493 cm^{-1} (square symbol solid line curve) and CO peak (empty circle line curve) in the operando Raman spectra of the 1st cycle are indicated (right *y*-axis). These peak intensities were determined from Raman spectra collected for 10 s while scanning the electric potential at a scan rate of 1 $mV\,s^{-1}$ (so that each spectrum corresponds to a potential range of 10 mV only) The second cycle show no CO and CuCarHyd bands, therefore omitted for clarity. Redox wave assignment: 1. reduction of CuCarHyd (the dashed line indicates the underlying reduction wave under 2); 2. reduction of Cu hydroxide; 3. Cu oxidation.

reaction consumes the material already present on the electrode, which is not re-formed in the subsequent oxidation/reduction waves, as discussed further below. In Figure 9 the irreversibility of the cathodic wave **1** is even more accentuated, suggesting the assignment to CuCarHyd reduction. Furthermore, in Figure S27 the first cycle of the cyclic voltammograms of the three different foam preparations (I, II, and III) measured in CO_2-free 0.1 M KOH are compared. The two reduction peaks in the first cycle of the CVs of malachite are again attributed to the reduction of Cu carbonate hydroxide and Cu hydroxide, while in the hydroxide-enriched sample and Cu foam sample, there is only one reduction peak that is attributed to the reduction of Cu hydroxide. Therefore, we propose the assignment of the CV redox waves as indicated in the Figures (labels **1**–**4** in Figure 8 and **1**–**3** in Figure 9). Briefly, cathodic wave **1** and wave **2** are attributed to the reduction of CuCarHyd and hydroxide, the anodic waves **3** from 0.5 to 0.9 V_{RHE} to the oxidation of Cu, and the uncommon anodic wave **4**, in the backwards sweep, at 0.7 V_{RHE}, is attributed to pitting corrosion, in line with previous assignments.[44]

CuCarHyd formation traced by CV Raman spectroscopy

Verification on the above CV-wave assignments and hints regarding relevance for CO_2RR are provided by analysis of the Raman spectra collected during the CV. The original Raman spectra are shown in Figures S28 and S29. In Figure 8 and Figure 9, the trends are summarized by reporting the amplitudes of the peaks of interest: the 1530 cm^{-1} peak, assigned to copper carbonate hydroxide, and the CO peak at near 2000 cm^{-1}. In Figure 8 (standard Cu foam cycled in CO_2-free bicarbonate solution), the assumed copper carbonate hydroxide bands (peak D at 1530 cm^{-1}) appear always at about 0.4 V_{RHE} and starts decaying below −0.1 V_{RHE} in the first CV cycle and below 0.1 V_{RHE} in the second cycle. In the same range of potentials, while the CuCarHyd peak decays, the magnitude of the CO peak rises, indicating a correlation between the two phenomena.

In Figure 9 (malachite-enriched Cu foam in CO_2-free KOH), the CuCarHyd peak is present from the beginning of the voltammogram, as expected, and it stays quite constant until the onset potential of reduction of the copper carbonate hydroxide at approximately −0.1 V_{RHE}, where the peak magnitude starts decaying to reach about zero at around −0.45 V_{RHE}; concurrently the CO peak rises from zero to its maximum amplitude at around −0.1 V_{RHE}. Again, the rising of the CO peak is associated with the disappearance of the CuCarHyd signal.

The experiments of Figure 8 suggest that CuCarHyd material, able to produce CO, can be formed in situ starting from oxidized Cu foam electrode in a solution of bicarbonate in absence of CO_2. This is evident by the fact that the CuCarHyd signal appears starting from zero amplitude, it disappears fully at negative potentials and reappears after the oxidation cycle. A further confirmation that the material we are proposing is a CuCarHyd is that in both system the CuCarHyd peaks disappear and CO forms at about the same potential (at −0.1 to −0.2 V_{RHE}).

CO formation by reduction of carbonate ions from CuCarHyd

We observe formation of CO in a situation where the only carbon source is malachite (see Figure 9). This finding implies CO formation by reduction of the carbonate ions of the Cu carbonate hydroxides. The CO formation occurs at similar and surprisingly low overpotentials when starting from the malachite-enriched Cu foam in KOH and the standard Cu foam in carbonate electrolyte. On these grounds we propose that a common route of CO formation though Cu carbonate hydroxides, which are initially present in the malachite enriched Cu foam but transiently formed at the standard Cu surface in the presence of a carbonate electrolyte.

As discussed further above, we assume that the formation of the copper carbonate hydroxide by the conversion of copper (hydro)oxides is supported by a high local pH at the electrode surface during the (hydro)oxide reduction (cathodic wave **2** in Figure 8). Moreover, we propose that CuCarHyd under operation conditions is formed by a non-equilibrium process involving the electrochemical-potential gradient between negative electrode and solution potential (see Figure 6B). CuCarHyd can withstand more negative potentials compared to the oxide (see 1st vs. 2nd cycle cathodic currents in Figure 9). The observation that the CuCarHyd is the last species that is detected going towards catalytic potentials and immediately prior CO production, suggests that the CuCarHyd could be an essential reaction intermediate of the CO_2RR.

Similar CV/Raman experiments were performed for hydroxide-enriched sample (Figure S30) together with malachite enriched one (Figure S31) and the usual Cu foam, with the aim to vary the amount of CuCarHyd formed and correlate it with the produced CO that is adsorbed at the catalyst electrode. The CO peak area trend vs. potential of the first cycle of CV/Raman is plotted for all three samples in Figure 10. The malachite sample produces the most Cu-bound CO at about

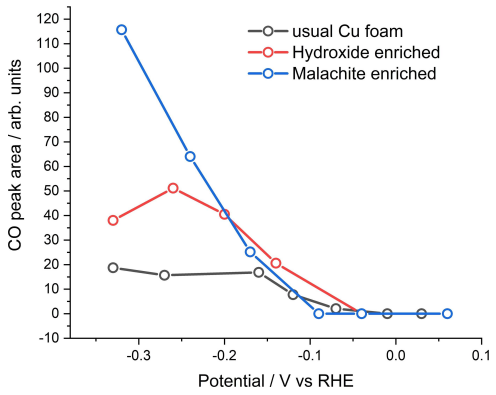

Figure 10. CO peak area trend versus potential of Raman data during first cycle of CV 1 mV s^{-1} in N_2-saturated 0.5 M $KHCO_3$ (pH 8.7) for Cu foam, hydroxide-enriched, and malachite-enriched sample.

−0.3 V_{RHE}, whereas the hydroxide enriched sample produced an intermediate CO quantity when compared to the standard Cu foam. On the other hand, removing the oxide layer by reducing the catalyst prior operation can shifts appearance of the CO peak to more negative potentials and reduces its magnitude (see Supporting Information section 13, Figures S32–S37). These correlations support the role of CuCarHyd species as a precursor of electrocatalytic CO formation.

Motivated by the experimental findings of our investigation, we propose that the starting state of CO_2 reduction in oxide-derived copper materials is the carbonate ion bound via oxygen atoms to Cu ions, which are not part of well-ordered metal surface. Figure 11 contrast the "conventional" binding mode of CO_2 in CO_2RR, that is, binding (adsorption) of the CO_2 molecule via its carbon atom to a well-ordered metallic surface (Figure 11A), with potential binding modes of the carbonate ion via two or three of its oxygen atoms (Figure 11B, C). At the level of working hypotheses, we see two options for the carbonate binding sites. First, they may be specific irregular residuals of the transformation of copper oxides into predominately metallic copper, in line with the special performance characteristic of oxide-derived Cu electrodes,[7,9–10,15a] among others assigned to grain boundary effects,[12] as well as performance difference when comparing various facets of metallic copper.[3a]

The second option involves dynamic formation of non-metallic phases also in the catalytic potential regime, as schematically summarized in Figure 11D. We hypothesize that the CuO_x/malachite system could function as a dynamic catalytic system for CO production, even at (negative) potential where the malachite material is not long-term stable. This is under the assumption that the reduction of the carbonate moieties in the CuCarHyd structure are kinetically more susceptible to reduction than the Cu^{2+} ions stabilized by a malachite-like ligand environment. This enables a catalytic cycle as depicted in Figure 11D, where the CuO_x formed after the reduction of the carbonate to CO slowly acquires a new carbonate ion and form a new CuCarHyd moiety, thus repeating the cycle. The metastable CuO_x/malachite catalyst eventually may become reduced to metallic Cu but, in the meantime, it might have undergone multiple turnovers of the catalytic cycle. This hypothesis is supported by, first, the known chemical inertia of malachite materials (indeed proposed as passivating layer in Cu electrodes), and second, the oxidative environment of the bulk solution, which can favor the CuCarHyd metastability, possibly involving a dynamic process of Cu ion dissolution and malachite re-formation close the metallic electrode. The outlined metastability may be supported significantly by local alkalinization, which could hinder CuO_x reduction (which needs a proton donor to occur) in favor of the acquisition of a new (bi)carbonate by CuO_x.

We are aware that the above scenarios are highly hypothetical in character; many questions remain open. Nevertheless, the perspective of a new mechanistic pathway in CO_2RR offered by this study may motivate future research aimed at understanding the full nature of the phenomena described here.

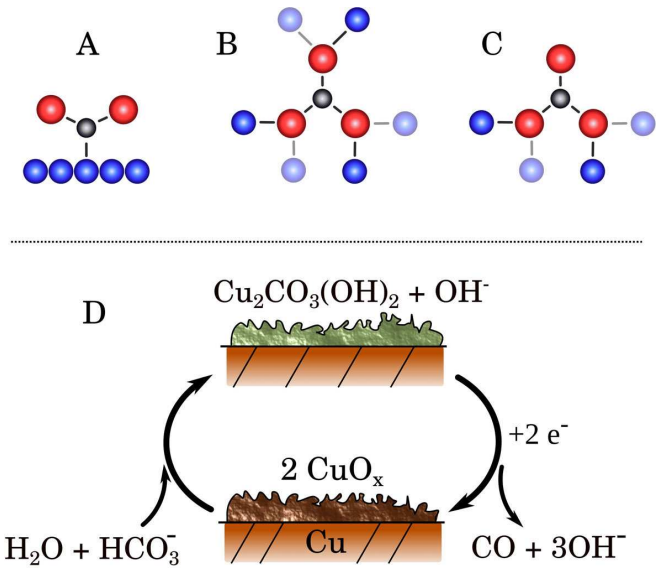

Figure 11. Carbon binding at the initial stage of CO_2 reduction. (A) binding (adsorption) of CO_2 molecules to a metallic copper surface via carbon atoms. (B, C) Proposed binding of carbonate ions in oxide-derived copper materials, with CO_3^{2-} bound via two or three oxygen atoms. (D) Proposed role of CuCarHyd in the catalytic reduction of carbonate ions. The brown and green cartoon structures indicate amorphous layers that are loosely bound to metallic Cu. The indicated stoichiometries are precise only for $x = 1$. Yet CuO_x may also represent an amorphous copper (hydr)oxide with different (non-integer) stoichiometries in the shown reaction cycle. In (B–D) the conversion of gaseous CO_2 to carbonate ions is omitted for clarity.

Conclusion

The results of our study motivate new perspectives regarding the catalytically active material and the basic mode of catalysis in CO_2 reduction reaction (CO_2RR) at Cu electrodes, as summarized in the following.

Experimental Section

Formation of Cu carbonate hydroxides

We show that copper carbonate hydroxide (CuCarHyd) does not need to be synthesized explicitly, but it is spontaneously produced once the electrode (coated with Cu_xOH_y) is immersed in bicarbonate solution (Figures 2–4, Figure 8). The presence of the copper carbonate hydroxide at catalytic potentials can be rationalized by local alkalization in combination with electrochemical potential gradients (Figure 6B), which could enable the formation of metastable materials over a large range of potentials (Figure 6A). The presence of oxidized species at highly reducing potentials (up to −1.0 V_{RHE}) indeed has been reported before for Cu-based CO_2RR systems, where Cu oxide residues were found to persist.[7a,9b,14a,b,45] We propose that also CuCarHyd are present at low overpotentials and may present at catalytic potentials, as a metastable material, partially consumed and re-synthesized in a cyclic fashion.

CO formation from CuCarHyd

The hypothesis of a CuCarHyd being the actual catalytic material of the CO_2RR has been considered before.[28–29,46] We show that in carbonate-free KOH and CO_2-depleted $KHCO_3$ solutions, the carbonate ions present in a CuCarHyd layer can be reduced to CO at the Cu-electrolyte interface (Figure 8, 9) and that increasing CuCarHyd amount increases the Raman signal of the produced CO (Figure 10). These experiments do not only support a crucial role of CuCarHyd. They also suggest that CO_2 reduction at the Cu foam electrodes does not necessarily start from CO_2, as mostly assumed, but can originate from carbonate ions as well, in line with the Raman spectra detected for ^{13}C isotope labelling of either CO_2 or carbonate (Figures 4, S8, S10).

Possible role of Cu oxides

The CuCarHyd likely is produced by the reaction of Cu oxide/hydroxide with dissolved bicarbonate/carbonate ions. This hypothesis on the genesis of the CuCarHyd that promote CO formation resonates with previous studies where Cu oxide has been proposed to favor CO_2 reduction.[7,9,10,15a,45b,47] For example, in a recent report high catalytic activity was observed for Cu electrodes that were positively polarized for a brief period of time, thereby reactivating maximal CO_2RR;[48] the positive polarization could restore the layer of oxide needed to react with bicarbonate to produce the CuCarHyd. In summary, the promoting role of Cu oxide in CO_2RR could relate to Cu oxide being a precursor to CuCarHyd.

Passivating role of CuCarHyd

It has been reported that CuCarHyd material could hinder the CO_2RR[15a] whereas our finding suggests a promoting role. Passivation behavior may arise from especially extended malachite formation on Cu electrode, as we observed for Cu foams with high abundance of CuCarHyd operating in carbonate buffer (see Figures S38, S39).

Alternative twist of CO_2RR mechanism

The above results on copper carbonate hydroxide layers suggest a basic mode of CO_2/carbonate reduction at Cu electrodes that contrast previous mechanistic models, as detailed in form of two hypothetical scenarios discussed in the context of Figure 11. We emphasize that the ultimate source of carbon remains CO_2that feeds the electrolyzer system via the CO_2/bicarbonate equilibrium, but the starting compound for CO_2 reduction would be the carbonate ion. High kinetic competence of the suggested carbonate-reduction step is indicated by CO formation already at surprisingly low overpotentials, as low as $-0.1\ V_{RHE}$, though CO desorption likely requires higher overpotentials.[13] We note that the here suggested CO_2RR routes may also relate the high catalytic activity of Cu-based materials towards $C_{1+n}>C_1$ products,[7b,9b,45b,49] since copper carbonate hydroxide structures could promote the C_1–C_1 intermediate interaction by high density of carbonate moieties in the structure.

Sample preparation

A Cu foam electrode was electrodeposited as described previously.[13] Briefly, the Cu foam electrode was deposited via electroreduction from a 0.2 M $CuSO_4$ solution at the cathode at a constant current density of $0.5\ A\,cm^{-2}$ applied for 20 s. After deposition, the electrode was rinsed with Milli-Q water and dried in air.

Operando Raman experiments

Raman spectra were acquired by a Renishaw in Via confocal Raman spectrometer. A 633 nm laser was used as scattering source with a power of 1.3 mW; the laser was focused (by a cylindrical lens) to a line on the Cu surface resulting in an illuminated spot of about 100 μm length and 10 μm width. A water immersion objective was used with 40× magnification ratio and numerical aperture (NA) of 0.8 and focal length of 3 mm.

Operando Raman experiments were performed in a home-built Raman cell (Figure S40), in which the horizontal working electrode faces the immersed objective. A Pt ring surrounding the working electrode was used as counter electrode, and a miniature Ag/AgCl electrode as the reference electrode. Potential measured vs. Ag/AgCl were converted to the RHE scale according to Equation (1):

$$V_{RHE} = V_{ref} + 0.2\ V + 0.059\ V \times pH \quad (1)$$

After mounting the catalyst in the cell, 10 mL electrolyte was purged with CO_2 or N_2 for 10 or 20 min, respectively, and subsequently poured into the cell, which then was left purging throughout the experiment. Spectra under OCP were always acquired first; the OCP for all the measurement was always around $0.5\ V_{RHE}$. Usually, two ranges of spectra were acquired separately, 106–1967 and 1926–3384 cm^{-1}, and after data analysis (described further below) presented as a single spectrum. Five accumulations were averaged per spectrum; the data collection time was 5 s for each accumulation. Raman spectra while scanning a CV with $1\ mV\,s^{-1}$ were acquired with two accumulations per spectrum only so that the each shown spectrum corresponds to a potential range of 10 mV (or ±5 mV). The data analysis approach has been described in our previous work;[21] in summary, the surface-plasmon background amplitude was subtracted and its average amplitude was used for normalization. The Figures finally shown in the text were plotted with an offset for clarity.

Materials

$KHCO_3$, K_2CO_3, and $KH^{13}CO_3$ (98% ^{13}C) were purchased from Sigma Aldrich, and KOH was purchased from Carl Roth. All chemicals were used without further treatment. Phosphate buffer was prepared by mixing 0.1 M KH_2PO_4 and K_2HPO_4 (Carl Roth) solution until the pH reached 6.8. All buffers were prepared with Milli-Q water (> 18 MΩ·cm). N_2 gas (purity 99.8%), CO_2 gas (purity 99.995%), and $^{13}CO_2$ gas (99.0% ^{13}C) were purchased from Linde Gas. D_2O (99.8% D) was purchased from Carl Roth.

Acknowledgements

We acknowledge financial support from the Bundesministerium für Bildung und Forschung (BMBF; CO2EKAT and Operando-XAS projects) and the China Scholarship Council (CSC, Ph.D. fellowship to S. J.). L. D. thanks the Swedish Research Council for economic support (grant No. 2019-00663). This research was further supported by the Alexander-von-Humboldt (AvH) foundation (postdoctoral fellowship awarded to L. D.). The X-ray absorption experiments have been pursued at the beamline KMC-3 of the Berlin synchrotron radiation source (BESSY) operated by the Helmholtz-Zentrum Berlin (HZB). We thank all the involved HZB colleagues for supporting the X-ray experiments. We gratefully acknowledge Fan Yang, Stefan Mebs, Michael Haumann, and

Ivelina Zaharieva for their support in X-ray data collection and analysis.

Conflict of Interest

The authors declare no conflict of interest.

Data Availability Statement

The data that support the findings of this study are available from the corresponding author upon reasonable request.

Keywords: CO_2 reduction reaction · electrocatalysis · electrode materials · operando spectroscopy · Raman spectroscopy

[1] a) O. Hoegh-Guldberg, D. Jacob, M. Taylor, T. Guillen Bolanos, M. Bindi, S. Brown, I. A. Camilloni, A. Diedhiou, R. Djalante, K. Ebi, F. Engelbrecht, J. Guiot, Y. Hijioka, S. Mehrotra, C. W. Hope, A. J. Payne, H. O. Portner, S. I. Seneviratne, A. Thomas, R. Warren, G. Zhou, *Science* **2019**, *365*, eaaw6974; b) G. A. Olah, G. K. Prakash, A. Goeppert, *J. Am. Chem. Soc.* **2011**, *133*, 12881–12898; c) R. Eisenberg, H. B. Gray, G. W. Crabtree, *Proc. Natl. Acad. Sci. USA* **2020**, *117*, 12543–12549.

[2] a) P. De Luna, C. Hahn, D. Higgins, S. A. Jaffer, T. F. Jaramillo, E. H. Sargent, *Science* **2019**, *364*, eaav3506; b) O. S. Bushuyev, P. De Luna, C. T. Dinh, L. Tao, G. Saur, J. van de Lagemaat, S. O. Kelley, E. H. Sargent, *Joule* **2018**, *2*, 825–832; c) S. C. Peter, *ACS Energy Lett.* **2018**, *3*, 1557–1561.

[3] a) Y. Hori, in *Modern Aspects of Electrochemistry, Vol. 42*, Springer, **2008**; b) A. Bagger, W. Ju, A. S. Varela, P. Strasser, J. Rossmeisl, *ChemPhysChem* **2017**, *18*, 3266–3273; c) S. Nitopi, E. Bertheussen, S. B. Scott, X. Liu, A. K. Engstfeld, S. Horch, B. Seger, I. E. L. Stephens, K. Chan, C. Hahn, J. K. Norskov, T. F. Jaramillo, I. Chorkendorff, *Chem. Rev.* **2019**, *119*, 7610–7672; d) S. Popović, M. Smiljanić, P. Jovanovič, J. Vavra, R. Buonsanti, N. Hodnik, *Angew. Chem. Int. Ed.* **2020**, *59*, 14736–14746; *Angew. Chem.* **2020**, *132*, 14844–14854.

[4] K. P. Kuhl, E. R. Cave, D. N. Abram, T. F. Jaramillo, *Energy Environ. Sci.* **2012**, *5*, 7050.

[5] a) C. Xie, Z. Niu, D. Kim, M. Li, P. Yang, *Chem. Rev.* **2020**, *120*, 1184–1249; b) D. Gao, I. Zegkinoglou, N. J. Divins, F. Scholten, I. Sinev, P. Grosse, B. Roldan Cuenya, *ACS Nano* **2017**, *11*, 4825–4831; c) X. Wang, K. Klingan, M. Klingenhof, T. Moller, J. Ferreira de Araujo, I. Martens, A. Bagger, S. Jiang, J. Rossmeisl, H. Dau, P. Strasser, *Nat. Commun.* **2021**, *12*, 794.

[6] a) S. Zhu, E. P. Delmo, T. Li, X. Qin, J. Tian, L. Zhang, M. Shao, *Adv. Mater.* **2021**, *33*, 2005484; b) A. Vasileff, C. Xu, Y. Jiao, Y. Zheng, S.-Z. Qiao, *Chem* **2018**, *4*, 1809–1831.

[7] a) S. Y. Lee, H. Jung, N. K. Kim, H. S. Oh, B. K. Min, Y. J. Hwang, *J. Am. Chem. Soc.* **2018**, *140*, 8681–8689; b) R. M. Arán-Ais, F. Scholten, S. Kunze, R. Rizo, B. Roldan Cuenya, *Nat. Energy* **2020**, *5*, 317–325.

[8] a) Y. Y. Birdja, E. Pérez-Gallent, M. C. Figueiredo, A. J. Göttle, F. Calle-Vallejo, M. T. M. Koper, *Nat. Energy* **2019**, *4*, 732–745; b) G. M. Tomboc, S. Choi, T. Kwon, Y. J. Hwang, K. Lee, *Adv. Mater.* **2020**, *32*, e1908398; c) T. K. Todorova, M. W. Schreiber, M. Fontecave, *ACS Catal.* **2019**, *10*, 1754–1768; d) A. A. Peterson, F. Abild-Pedersen, F. Studt, J. Rossmeisl, J. K. Nørskov, *Energy Environ. Sci.* **2010**, *3*, 1311–1315; e) Y. Zheng, A. Vasileff, X. Zhou, Y. Jiao, M. Jaroniec, S.-Z. Qiao, *J. Am. Chem. Soc.* **2019**, *141*, 7646–7659.

[9] a) C. W. Li, J. Ciston, M. W. Kanan, *Nature* **2014**, *508*, 504–507; b) H. Jung, S. Y. Lee, C. W. Lee, M. K. Cho, D. H. Won, C. Kim, H. S. Oh, B. K. Min, Y. J. Hwang, *J. Am. Chem. Soc.* **2019**, *141*, 4624–4633; c) H. Mistry, A. S. Varela, C. S. Bonifacio, I. Zegkinoglou, I. Sinev, Y. W. Choi, K. Kisslinger, E. A. Stach, J. C. Yang, P. Strasser, B. R. Cuenya, *Nat. Commun.* **2016**, *7*, 12123.

[10] a) J. Wang, H. Y. Tan, Y. Zhu, H. Chu, H. M. Chen, *Angew. Chem. Int. Ed.* **2021**, *133*, 2–16; b) J. E. Pander, D. Ren, Y. Huang, N. W. X. Loo, S. H. L. Hong, B. S. Yeo, *ChemElectroChem* **2018**, *5*, 219–237; c) L. Mandal, K. R. Yang, M. R. Motapothula, D. Ren, P. Lobaccaro, A. Patra, M. Sherburne, V. S. Batista, B. S. Yeo, J. W. Ager, J. Martin, T. Venkatesan, *ACS Appl. Mater. Interfaces* **2018**, *10*, 8574–8584.

[11] a) J. H. Montoya, C. Shi, K. Chan, J. K. Norskov, *J. Phys. Chem. Lett.* **2015**, *6*, 2032–2037; b) F. Calle-Vallejo, M. T. Koper, *Angew. Chem. Int. Ed.* **2013**, *52*, 7282–7285; *Angew. Chem.* **2013**, *125*, 7423–7426.

[12] A. Verdaguer-Casadevall, C. W. Li, T. P. Johansson, S. B. Scott, J. T. McKeown, M. Kumar, I. E. Stephens, M. W. Kanan, I. Chorkendorff, *J. Am. Chem. Soc.* **2015**, *137*, 9808–9811.

[13] K. Klingan, T. Kottakkat, Z. P. Jovanov, S. Jiang, C. Pasquini, F. Scholten, P. Kubella, A. Bergmann, B. Roldan Cuenya, C. Roth, H. Dau, *ChemSusChem* **2018**, *11*, 3449–3459.

[14] a) F. Cavalca, R. Ferragut, S. Aghion, A. Eilert, O. Diaz-Morales, C. Liu, A. L. Koh, T. W. Hansen, L. G. M. Pettersson, A. Nilsson, *J. Phys. Chem. C* **2017**, *121*, 25003–25009; b) A. Eilert, F. Cavalca, F. S. Roberts, J. Osterwalder, C. Liu, M. Favaro, E. J. Crumlin, H. Ogasawara, D. Friebel, L. G. Pettersson, A. Nilsson, *J. Phys. Chem. Lett.* **2017**, *8*, 285–290; c) Marco Favaro, Hai Xiao, T. Cheng, W. A. Goddard III, J. Yano, E. J. Crumlin, *Proc. Natl. Acad. Sci. USA* **2017**, *114*, 6706–6711.

[15] a) J.-J. Velasco-Vélez, T. Jones, D. Gao, E. Carbonio, R. Arrigo, C.-J. Hsu, Y.-C. Huang, C.-L. Dong, J.-M. Chen, J.-F. Lee, P. Strasser, B. Roldan Cuenya, R. Schlögl, A. Knop-Gericke, C.-H. Chuang, *ACS Sustainable Chem. Eng.* **2018**, *7*, 1485–1492; b) S. C. Lin, C. C. Chang, S. Y. Chiu, H. T. Pai, T. Y. Liao, C. S. Hsu, W. H. Chiang, M. K. Tsai, H. M. Chen, *Nat. Commun.* **2020**, *11*, 3525.

[16] H. Xiao, W. A. Goddard, 3rd, T. Cheng, Y. Liu, *Proc. Natl. Acad. Sci. USA* **2017**, *114*, 6685–6688.

[17] a) X. Li, S. Wang, L. Li, Y. Sun, Y. Xie, *J. Am. Chem. Soc.* **2020**, *142*, 9567–9581; b) A. D. Handoko, F. Wei, Jenndy, B. S. Yeo, Z. W. Seh, *Nat. Catal.* **2018**, *1*, 922–934; c) J. Li, J. Gong, *Energy Environ. Sci.* **2020**, *13*, 3748–3779; d) Y. Zhu, J. Wang, H. Chu, Y.-C. Chu, H. M. Chen, *ACS Energy Lett.* **2020**, *5*, 1281–1291; e) S. Zhu, T. Li, W.-B. Cai, M. Shao, *ACS Energy Lett.* **2019**, *4*, 682–689; f) R. Kas, O. Ayemoba, N. J. Firet, J. Middelkoop, W. A. Smith, A. Cuesta, *ChemPhysChem* **2019**, *20*, 2904–2925; g) Y. Deng, B. S. Yeo, *ACS Catal.* **2017**, *7*, 7873–7889.

[18] a) N. Heidary, K. H. Ly, N. Kornienko, *Nano Lett.* **2019**, *19*, 4817–4826; b) B. Sharma, R. R. Frontiera, A.-I. Henry, E. Ringe, R. P. Van Duyne, *Mater. Today* **2012**, *15*, 16–25.

[19] a) J. Langer, D. Jimenez de Aberasturi, J. Aizpurua, R. A. Alvarez-Puebla, B. Auguie, J. J. Baumberg, G. C. Bazan, S. E. J. Bell, A. Boisen, A. G. Brolo, J. Choo, D. Cialla-May, V. Deckert, L. Fabris, K. Faulds, F. J. Garcia de Abajo, R. Goodacre, D. Graham, A. J. Haes, C. L. Haynes, C. Huck, T. Itoh, M. Kall, J. Kneipp, N. A. Kotov, H. Kuang, E. C. Le Ru, H. K. Lee, J. F. Li, X. Y. Ling, S. A. Maier, T. Mayerhofer, M. Moskovits, K. Murakoshi, J. M. Nam, S. Nie, Y. Ozaki, I. Pastoriza-Santos, J. Perez-Juste, J. Popp, A. Pucci, S. Reich, B. Ren, G. C. Schatz, T. Shegai, S. Schlucker, L. L. Tay, K. G. Thomas, Z. Q. Tian, R. P. Van Duyne, T. Vo-Dinh, Y. Wang, K. A. Willets, C. Xu, H. Xu, Y. Xu, Y. S. Yamamoto, B. Zhao, L. M. Liz-Marzan, *ACS Nano* **2020**, *14*, 28–117; b) S.-Y. Ding, J. Yi, J.-F. Li, B. Ren, D.-Y. Wu, R. Panneerselvam, Z.-Q. Tian, *Nat. Rev. Mater.* **2016**, *1*, 1–16; c) S. Schlucker, *Angew. Chem. Int. Ed.* **2014**, *53*, 4756–4795; *Angew. Chem.* **2014**, *126*, 4852–4894.

[20] a) C. M. Gunathunge, X. Li, J. Li, R. P. Hicks, V. J. Ovalle, M. M. Waegele, *J. Phys. Chem. C* **2017**, *121*, 12337–12344; b) Y. Zhao, X. Chang, A. S. Malkani, X. Yang, L. Thompson, F. Jiao, B. Xu, *J. Am. Chem. Soc.* **2020**, *142*, 9735–9743; c) A. Wuttig, C. Liu, Q. Peng, M. Yaguchi, C. H. Hendon, K. Motobayashi, S. Ye, M. Osawa, Y. Surendranath, *ACS Cent. Sci.* **2016**, *2*, 522–528; d) G. Iijima, T. Inomata, H. Yamaguchi, M. Ito, H. Masuda, *ACS Catal.* **2019**, *9*, 6305–6319.

[21] S. Jiang, K. Klingan, C. Pasquini, H. Dau, *J. Chem. Phys.* **2019**, *150*, 041718.

[22] I. V. Chernyshova, P. Somasundaran, S. Ponnurangam, *Proc. Natl. Acad. Sci. USA* **2018**, *115*, E9261–E9270.

[23] I. V. Chernyshova, S. Ponnurangam, *Phys. Chem. Chem. Phys.* **2019**, *21*, 8797–8807.

[24] M. Dunwell, Q. Lu, J. M. Heyes, J. Rosen, J. G. Chen, Y. Yan, F. Jiao, B. Xu, *J. Am. Chem. Soc.* **2017**, *139*, 3774–3783.

[25] S. Zhu, B. Jiang, W. B. Cai, M. Shao, *J. Am. Chem. Soc.* **2017**, *139*, 15664–15667.

[26] R. Kortlever, K. H. Tan, Y. Kwon, M. T. M. Koper, *J. Solid State Electrochem.* **2013**, *17*, 1843–1849.

[27] a) Y. Hori, A. Murata, R. Takahashi, *J. Chem. Soc. Faraday Trans. 1* **1989**, *85*, 2309–2326; b) Y. Hori, A. Murata, R. Takahashi, S. Suzuki, *J. Chem. Soc. Chem. Commun.* **1988**, 17–19.

[28] M. Spodaryk, K. Zhao, J. Zhang, E. Oveisi, A. Züttel, *Electrochim. Acta* **2019**, *297*, 55–60.

[29] A. Eilert, F. S. Roberts, D. Friebel, A. Nilsson, *J. Phys. Chem. Lett.* **2016**, *7*, 1466–1470.
[30] a) A. Baudler, I. Schmidt, M. Langner, A. Greiner, U. Schröder, *Energy Environ. Sci.* **2015**, *8*, 2048–2055; b) J. Y. Lee, K. D. Karlin, *Curr. Opin. Chem. Biol.* **2015**, *25*, 184–193; c) A. D. Sekar, T. Jayabalan, H. Muthukumar, N. I. Chandrasekaran, S. N. Mohamed, M. Matheswaran, *Energy* **2019**, *172*, 173–180.
[31] M. Dunwell, W. Luc, Y. Yan, F. Jiao, B. Xu, *ACS Catal.* **2018**, *8*, 8121–8129.
[32] Y. Deng, A. D. Handoko, Y. Du, S. Xi, B. S. Yeo, *ACS Catal.* **2016**, *6*, 2473–2481.
[33] A. R. Davis, B. G. Oliver, *J. Solution Chem.* **1972**, *1*, 329–339.
[34] a) A. S. Malkani, M. Dunwell, B. Xu, *ACS Catal.* **2018**, *9*, 474–478; b) B. D. Smith, D. E. Irish, P. Kedzierzawski, J. Augustynski, *J. Electrochem. Soc.* **1997**, *144*, 4288; c) L. Wang, K. Gupta, J. B. M. Goodall, J. A. Darr, K. B. Holt, *Faraday Discuss.* **2017**, *197*, 517–532; d) J. Gao, H. Zhang, X. Guo, J. Luo, S. M. Zakeeruddin, D. Ren, M. Gratzel, *J. Am. Chem. Soc.* **2019**, *141*, 18704–18714.
[35] G. Niaura, A. K. Gaigalas, V. L. Vilker, *J. Phys. Chem. B* **1997**, *101*, 9250–9262.
[36] a) C. A. Melendres, F. Hahn, G. A. Bowmaker, *Electrochim. Acta* **2000**, *46*, 9–13; b) C. Schlaup, S. Horch, *Surf. Sci.* **2013**, *608*, 44–54.
[37] R. L. Frost, W. N. Martens, L. Rintoul, E. Mahmutagic, J. T. Kloprogge, *J. Raman Spectrosc.* **2002**, *33*, 252–259.
[38] K. Arihara, Fusao Kitamura, Takeo Ohsaka, K. Tokuda, *J. Electroanal. Chem.* **2001**, *510*, 1280135.
[39] a) M. Moradzaman, G. Mul, *ChemElectroChem* **2021**, *8*, 1478–1485; b) Z. M. Detweiler, J. L. White, S. L. Bernasek, A. B. Bocarsly, *Langmuir* **2014**, *30*, 7593–7600; c) M. F. Baruch, J. E. Pander, J. L. White, A. B. Bocarsly, *ACS Catal.* **2015**, *5*, 3148–3156.
[40] a) J. F. Li, Y. J. Zhang, S. Y. Ding, R. Panneerselvam, Z. Q. Tian, *Chem. Rev.* **2017**, *117*, 5002–5069; b) J. A. Dieringer, A. D. McFarland, N. C. Shah, D. A. Stuart, A. V. Whitney, C. R. Yonzon, M. A. Young, X. Zhang, R. P. Van Duyne, *Faraday Discuss.* **2006**, *132*, 9–26; c) A. K. Singh, S. A. Khan, Z. Fan, T. Demeritte, D. Senapati, R. Kanchanapally, P. C. Ray, *J. Am. Chem. Soc.* **2012**, *134*, 8662–8669; d) W. Wei, S. Li, J. E. Millstone, M. J. Banholzer, X. Chen, X. Xu, G. C. Schatz, C. A. Mirkin, *Angew. Chem. Int. Ed.* **2009**, *48*, 4210–4212; *Angew. Chem.* **2009**, *121*, 4274–4276.
[41] J. B. Allen, R. F. Larry, *Electrochemical methods fundamentals and applications*, John Wiley & Sons, **2001**.
[42] B. W. Vink, *Mineral. Mag.* **1986**, *50*, 41–47.
[43] C. S. Hurlbut, C. Klein, *Manual of mineralogy (after James D. Dana)*, Wiley, **1977**.
[44] M. P. Sánchez, M. Barrera, S. Gonzalez, R. M. Souto, R. C. Salvarezza, A. J. Arvia, *Electrochim. Acta* **1990**, *35*, 1337–1343.
[45] a) D. Kim, S. Lee, J. D. Ocon, B. Jeong, J. K. Lee, J. Lee, *Phys. Chem. Chem. Phys.* **2015**, *17*, 824–830; b) P. De Luna, R. Quintero-Bermudez, C.-T. Dinh, M. B. Ross, O. S. Bushuyev, P. Todorović, T. Regier, S. O. Kelley, P. Yang, E. H. Sargent, *Nat. Catal.* **2018**, *1*, 103–110.
[46] D. A. Henckel, M. J. Counihan, H. E. Holmes, X. Chen, U. O. Nwabara, S. Verma, J. Rodríguez-López, P. J. A. Kenis, A. A. Gewirth, *ACS Catal.* **2020**, *11*, 255–263.
[47] C. J. Chang, S. F. Hung, C. S. Hsu, H. C. Chen, S. C. Lin, Y. F. Liao, H. M. Chen, *ACS Cent. Sci.* **2019**, *5*, 1998–2009.
[48] K. W. Kimura, R. Casebolt, J. Cimada DaSilva, E. Kauffman, J. Kim, T. A. Dunbar, C. J. Pollock, J. Suntivich, T. Hanrath, *ACS Catal.* **2020**, *10*, 8632–8639.
[49] a) W. Zhang, C. Huang, Q. Xiao, L. Yu, L. Shuai, P. An, J. Zhang, M. Qiu, Z. Ren, Y. Yu, *J. Am. Chem. Soc.* **2020**, *142*, 11417–11427; b) Y. Huang, A. D. Handoko, P. Hirunsit, B. S. Yeo, *ACS Catal.* **2017**, *7*, 1749–1756.

Manuscript received: November 26, 2021
Revised manuscript received: March 1, 2022
Accepted manuscript online: March 14, 2022
Version of record online: March 22, 2022